Article

Not peer-reviewed version

Carbon Dots Synthesis in CYTOP Optical Fiber Using IR Femtosecond Laser Direct Writing and Its Luminescence Properties

Ruyue QUE , Jean-Frédéric Audibert , Enrique Garcia-Caurel , Olivier Plantevin , Kyriacos Kalli , Matthieu Lancry , Bertrand Poumellec * , Robert B. Pansu

Posted Date: 22 March 2024

doi: 10.20944/preprints202403.1320.v1

Keywords: CYTOP fiber; femtosecond laser; laser induced modification; photoluminescence creation; multifunctionnal material

Article

Carbon Dots Synthesis in CYTOP Optical Fiber Using IR Femtosecond Laser Direct Writing and Its Luminescence Properties

Ruyue Que [1], Jean-Frédéric Audibert [1], Enrique Garcia-Caurel [2], Olivier Plantevin [3], Kyriacos Kalli [4], Matthieu Lancry [5], Bertrand Poumellec [5,*] and Robert B. Pansu [1]

[1] Université Paris-Saclay, CNRS, ENS Paris-Saclay, CentraleSupélec, LuMIn, 91190 Gif-sur-Yvette, France
[2] Institut Polytechnique de Paris, CNRS, École Polytechnique, LPICM, 91120 Palaiseau, France
[3] Université Paris-Saclay, CNRS, Laboratoire de Physique des Solides, 91405 Orsay, France
[4] Cyprus University of Technology, Nanophotonics Research Laboratory, 3036 Limassol, Cyprus
[5] Université Paris-Saclay, CNRS, Institut de Chimie Moléculaire et des Matériaux d'Orsay, 91405 Orsay, France
* Correspondence: Bertrand.Poumellec@universite-paris-saclay.fr

Abstract: Luminescent carbon dots (CDs) were locally synthesized in the core of CYTOP fibers using IR femtosecond laser direct writing (FLDW), a one-step simple method serving as a post-treatment of the genuine fiber. This approach enables the creation of several types of modifications such as ellipsoid voids. The CDs and photoluminescence (PL) distribute at the periphery of the voids. The PL spectral properties were studied through Excitation Emission Matrix in the visible range and excitation/emission spectrum in UV/visible range. Our finding reveals the presence of at least 3 distinct luminescent species, facilitating a broad excitation range extending from UV to green, and light emission spanning from blue to red. The average laser power and dose influence the quantity and ratio of these luminescent CD species. Additionally, we measured the spatially resolved lifetime of the luminescence during and after the irradiation. We found longer lifetimes at the periphery of the laser-induced modified regions and shorter ones closer to the center, with a dominant lifetime ~ 2ns. Notably, unlike many other luminophores, these laser-induced CDs are insensitive to oxygen, enhancing their potential for display or data storage applications.

Keywords: CYTOP fiber; femtosecond laser; laser induced modification; photoluminescence creation; multifunctionnal material

1. Introduction

Carbon dots (CDs) refer to a class of carbon-based nanomaterials, including graphene quantum dots (GQDs), carbon nanodots (CNDs), polymer dots (PDs) inter alia, having amorphous to nanocrystalline cores [1]. Before the discovery of CDs in early 2000s [2,3], conventional dyes and semiconductor quantum dots were commonly used [4,5]. However, their applications are restricted due to the utilization of highly hazardous heavy metal ions [6], which has led to the shift in interest towards CDs and a thorough analysis of them. They have recently received a lot of attention because of their unique properties like low toxicity, biocompatibility, chemical inertness, tunable fluorescence, flexible surface modification, and a wide range of applications like chemical sensing [7], bioimaging, biosensing [8], nanomedicine [9], photocatalysis [10], drug delivery [11], fluorescent probes [12], optoelectronic devices [13].

Currently, there are several methods available for synthesizing CDs. Generally, there are two strategies for synthesizing CDs: "top-down" which is cutting from different carbon sources such as graphite powder, carbon rods, carbon fibers, etc., and "bottom-up" synthesis from organic synthons or polymers and modification of surface functionality or passivation [1]. One step in the synthesis of CDs is the formation of fluorophores by the aromatization of the carbon cycles. These aromatization methods include pyrolysis synthesis [14], arc discharge [15], carbonization [16], solvothermal

 doi:10.20944/preprints202403.1320.v1

synthesis [17], hydrothermal [18–25], microwave [26], ultrasonication [27], electrochemical [28], chemical oxidation [29]. CDs fabricated by those methods can be process in a large quantity, but there are limitations when it comes to producing spatially resolved carbon dots or dedicated 3D fabrication inside materials. While embedding [30] or coating [31] can to some extent incorporate them into materials, they do not allow a spatial control of the CDs position.

IR femtosecond laser direct writing (FLDW) can produce spatially resolved CDs with a high degree of flexibility, aiming to overcome the limitations of traditional synthesis methods. This approach leverages the extremely high intensity at the focus of femtosecond lasers, leading to localized modifications through nonlinear absorption of Near-InfraRed (NIR) photons. Such attributes render FLDW a promising technique for 3D functional implementation in chips and optical fibers, such as nanogratings [32,33], nanocrystallizations [34], etc. Additionally, this method has already been used to create CDs in some materials such as PMMA, PDMS, PC [35], Cyclo Olefin Polymer (ZEONEX®) [36], amino acid single crystal [37], and even cells [38].

In this study, we have demonstrated that IR femtosecond laser direct writing (FLDW) can produce spatially resolved CDs in the core of a perfluorinated fiber of CYTOP. CYTOP (cyclic transparent optical polymer [39]), is a promising graded-index fiber, exhibiting low attenuation at telecom wavelengths [40] due to the replacement of C-H bonds with fluorocarbon groups (C-F), making it highly suitable for optical fiber applications. In addition, CYTOP is less sensitive to environmental influences, such as being insoluble in organic solutions and having low water absorption. The absence of residual optical absorption by CYTOP at the laser wavelength is a challenge that we overcome. The absence of CH bound in the CYTOP imply that we have produced perfluorinated carbon dots and this for the first time.

2. Experimental Details

2.1. Materials

The fibers used in this research are amorphous perfluorinated plastic optical fibers (POFs), designed and produced by Chromis Technologies. The type is CTL-S with -CF3 ends (refer to [39]). These fibers have a diameter of 90µm and are composed of a pure CYTOP cladding around a 62.5µm CYTOP graded-index core with dopants [41]. The overcladding, made of XYLEX® material (a blend of polycarbonate and an amorphous polyester), is removed by dissolving it in CH_2Cl_2 within a few minutes. The effective refractive index of these fibers is around 1.34 (at λ=589nm), with a higher index in the core. Further details are available in the product datasheet. CYTOP fibers exhibits high transparency in range UVA, UVB, visible and IR up to 2000nm. Specifically, the attenuation at 1030nm is 30 dB/km and absorption starts from 190nm (6.5eV) [42,43]. The amorphous transition temperature is 108ºC and thermal decomposition starts from 400ºC.

2.2. Carbon Dots Synthesis: fs Laser Irradiation

For the CDs fabrication, we used a Yb-doped fiber pulsed fs laser (Goji HP, Amplitude System) with a wavelength of 1030nm, a pulse duration of 165fs and an adjustable repetition rate (RR) ranging from 5MHz to 20MHz. The laser beam was focused into the core of the CYTOP fiber through an objective of 0.75NA (40x). The average power of the laser on the samples has been varied from 18.5mW to 703mW. The beam is linearly polarized along the fiber axis. Given that the CYTOP fiber has graded refractive index (RI) around 1.3395 in near IR, the fiber is immerged in a 5.6% Glycerol aqueous solution (n_D^{20}=1.3399) [44] as a phase matching solution to minimize the influences of the fiber shape and interface on the focusing. IR fs laser light diameter and divergence was adjusted using a beam expander (ZBE11, Thorlabs) to firstly cover all the pupil of the objective and secondly to adjust IR light focus plane to be the same as the observation visible light. A shutter with an openning time of 100ms was applied to control the irradiation exposure time.

 doi:10.20944/preprints202403.1320.v1

2.3. Raman Spectroscopy

To identify the nature of the species produced by the laser irradiation, Raman spectra of the CYTOP fiber in pristine and in irradiated luminescent regions were measured. Measurements were conducted under 780nm continuous laser by a Raman Microscope system (DXR, Thermo Scientific). The depolarized laser beam was focused on the sample with a microscope objective of magnification x50 with NA=0.5 or 0.75. The aperture of the pinhole was fixed to 50μm resulting in a spatial resolution of 1μm in the focal plane and 2μm in depth. Spectra were record from 3421cm^{-1} to 63cm^{-1} with an estimated spectral resolution from 4.7cm^{-1} to 8.7cm^{-1}. The probe laser power was set to be 5W and 10W. Exposure time was set to be from 5s to 15s. The averaging was set to be typically around 25 times. The removal of the fluorescence background from 3421cm^{-1} to 63cm^{-1} was done by adjusting the baseline with a 6th order polynomial. The spectra were then decomposed through Principal Components Analysis (PCA) method.

2.4. Transmission Electron Microscopy (TEM)

The irradiated fibers were embedding in Epon resin (Kit LV premix Medium, Agar Scientific AGR1165) and polymerized 24h at 60°C. Ultrathin sections were realized with an ultramicrotome (UC6, Leica Microsystems) and a 35° diamond knife (Diatome) through the fiber cross-section. Sections were collected on 200 mesh nickel formvar-carbon coated grids. Sections were imaged with a JEOL1400 operating at 120kV equipped with a RIO9 camera (Ametek).

2.5. PL Properties of CDs and Other Luminophores

Excitation at 515nm. 515nm excitation light is the Second Harmonic Generation (SHG) of the above irradiation IR laser, produced through a BBO crystal (β-BaB_2O_4) with phase matched angle. The excitation light is expanded into a collimated beam when illuminating the sample.

Lifetime measurement. Lifetime and the corresponding intensity decay were recorded as an image by a space- and time-resolved single photon counter (Photonscore GmbH). Photons are saved with their attributes (time and place) allowing multiple analysis of the data [45]. For testing the *environmental sensitivity of the luminescence,* O_2 environment was created by concealing the irradiated fibers in a glass bottle and flushing with O_2. 20 minutes of perfusion, all the air in the glass cylinder was replaced by O_2. The no-O_2 environmental was created by the same method but flushing with Ar.

Excitation spectra and Emission spectra by UV excitation were measured by spectrofluorometer (PTI QuantaMaster 8000). 75W Xe Arc-lamp from Quanta Master System (Horiba JY) was used as excitation light, wavelength selected by a single monochromator.

Excitation Emission Matrix (EEM) in the visible range. They were performed with a confocal microscope (Sp8-X, Leica) equipped with a white light pulsed supercontinuum source based on Photonics Crystal Fiber, with pulse duration of 120 fs and repetition rate of 80 MHz (NKT photonics). In this paper, the collection of light remains within a 12.5 ns window. The objective magnification was ×20 (oil immersion with 0.7NA). The optical axial spatial resolution with the pinhole (53.1 μm) of the confocal microscope system using 10x objective, is 565nm at λ=470nm and 675nm at λ=670nm. Excitation wavelength was varied from 470nm to 670nm with 8 nm step. The emission spectra were measured by a Hybrid photodetector (Leica HyD) from 494 nm to 694 nm with a 8 nm spectral resolution. Hybrid photodetectors, combining PMTs and avalanche photodiodes (APDs), having been used because it has a better sensitivity (47% instead of 25%) and lower level of dark noise compared to classic photomultiplier tubes (PMTs). Emission/excitation spectra matrix (EEM) were recorded for each pixel of the microscope image. However, small regions of interest (ROIs) are defined to perform local averaging for showing the difference from one position to another. Specifically, the EEM visualizes the energy level distribution of the luminophores. Associated with a principal component analysis, it gives the number of species, their associated spectra and their localization [36].

 doi:10.20944/preprints202403.1320.v1

3. Results

3.1. Fs laser Induced Modifications

A series of irradiation experiments were conducted to explore the synthesis conditions of carbon dots. The fs pulsed laser was focused on a fixed position within the fiber core. During exposure to the laser light, the material experienced various changes. We established thresholds and processing windows for these different permanent modifications relative to laser power (y-axis) and exposure time (x-axis), as illustrated in Figure 1(a). In these experiments, the laser powers were incrementally increased by 3.7mW steps from 37mW to 74mW. The exposure times were set by 100ms intervals starting from 100ms and up to 2.5s, followed by longer intervals of 0.5s until 5s. This variation allowed for an escalating cumulated dose. After irradiation with these laser conditions, we identified 3 types of modifications, defined by their distinct morphologies, as shown in Figure 1(b).

Type 1. It is the first stage of visible modification when exposed to fs laser light. It is observable at low power level, appearing as a black dot with the size of the beam waist diameter at $1/e^2$ (~1μm), as shown in Figure 1(b). During irradiation, this dot may exhibit slight movement within a 2μm radius.

Type 2. This stage is characterized by the formation of an ellipsoidal modified region. This region gradually enlarges over exposure time, pushing material outward and resulting in the formation of concentric rings of refractive index change around it, as shown in Figure 1(b). Occasionally, this process also produces a multifold spiral "galaxy" structure. This dynamic can be observed in a video in the supplementary section.

Type 3. This kind of modification occurs when the enlargement process of Type 2 continues to a point where the material cannot withstand the internal pressure and overcomes the rupture limit.

This observation suggests that the fs laser induced some gas to form a Type 2 cavity. From a top view of a Type 3 modification, as shown in Figure 1(b), the central black region is a tunnel rather than a spherical cavity. Inside this tunnel, structures inside resembling a lamprey's mouth are observed, which may be indicative of a rapid crystallization.

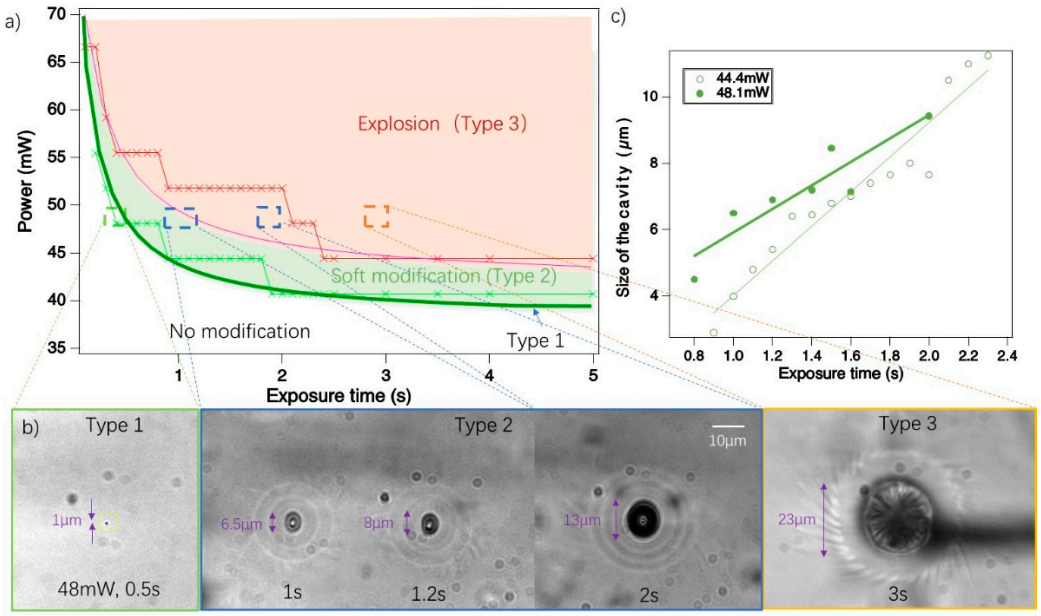

Figure 1. (a) Threshold profiles and process windows of modification types; green for Type 1 and 2, red for Type 3. Dark green and pink curve indicate the fixed dose of about 4mJ with offset 39 and 44mW, respectively. Small crosses mark experimental data. (b) Microscope images of modification types in transmission mode using natural light. Modification parameters corresponding to dashed frames in (a). (c) Cavity size and linearly fitting of Type 2 modifications versus exposure time for laser powers of 44.4mW (green) and 48.3mW (dark green).

 doi:10.20944/preprints202403.1320.v1

Figure 1(a) illustrate the boundaries and processing windows of these 3 modification types. Below 40mW, (pulse energy 4nJ at Repetition Rate 10MHz), no visible transitions are observed, regardless the exposure duration. In this parameter condition, especially for RR of 10MHz, the transition of Type 1 to Type 2 occurs rapidly. Consequently, the window to generate Type 1 is so narrow, appearing merely as a dividing line between the non-modified region and Type 2 modification. It corresponds to a dose of 5mJ, which is shown in Figure 1(a) by a thick green line. Type domain can be adjusted approximately by Power(mW)=39mJ+4mJ.s/exposure time(s). The size of the modified regions of Type 2 seems to linearly increase over exposure time in Figure 1(c). Type 3 modification boundaries can be adjusted by Power(mW)=44mJ+4mJ.s/exposure time(s).

3.2. Photoluminescence (PL) Properties

3D distribution and Excitation Emission Matrix in visible range. Photoluminescence (PL) has been detected in Type 2 and Type 3 modifications, indicating a chemical change in the molecules structure of the fiber. In the case of Type 2 modification, an increase in PL intensity is observed with the accumulation of more energy over time. However, prolonged exposure time or higher power can cause the Type 2 modified region to break, forming a Type 3 tunnel. In many instances, Type 3 have lower PL intensity compared to some big-size Type 2 modifications. This decrease may be due to the expulsion of luminescent matter during breakage. Note that in some cases Type 3 forms much faster under higher power, leaving insufficient time for the generation of luminescence species. This observation implies that optimal PL in Type 2 modifications can be achieved by fine tuning the laser parameters and timing to just before the transition to Type 3. Therefore, a “combo” method has been developed. This method involves initially applying power above the threshold to trigger Type 2 modifications, but with minimized exposure time for smaller modifications. Subsequently, power is reduced, and exposure time is distributed over multiple periods to gradually deliver energy.

Figure 2(b) and (a) illustrate the PL distribution of two Type 2 ROIs created under different laser parameters by confocal microscopy and its corresponding transmission image under natural light. ROI1 is a standard Type 2 modification (irradiated by 10MHz, 51.8mW during 2s), while ROI2 is a Type 2 modification using the ‘combo’ method (10MHz, 51.8mW during 2s, followed by 2 times of 18mw,100ms), denoted Type2+. This method enlarges the void and significantly increase PL intensity, i.e.,10 times greater than a typical Type 3 modifications. Figure 2(c) displays a screenshot of the top and side views of a 3D reconstruction of these 2 luminescent volumes, measured along the z-axis (10nm step). From Figure 2(b) and (c), we can see that in ROI1, the PL is distributed throughout the cavity with a slight layer texture, while ROI2 exhibits higher intensity around the periphery compared to the center. Note that in the side view of 3D images, the PL distribution is asymmetric along the vertical direction; it is an artifact of confocal microscopy, as the signal was disrupted during the measurement of planes behind the void. Therefore, the PL distribution in Type 2 and Type 2+ modifications are ‘solid’ and hollow ellipsoid, respectively. Since the image were measured simultaneously, it is evident that the ‘combo’ method creates more PL in ROI2. A similar PL creation by fs laser irradiation was observed in polyimide [46] , attributed to deposition on the inner surface after evaporation. However, in our study, the luminescent regions appear to be on the outer surface of the void, by comparing with the image Figure 2(a) and (b), as further corroborated by TEM results.

 doi:10.20944/preprints202403.1320.v1

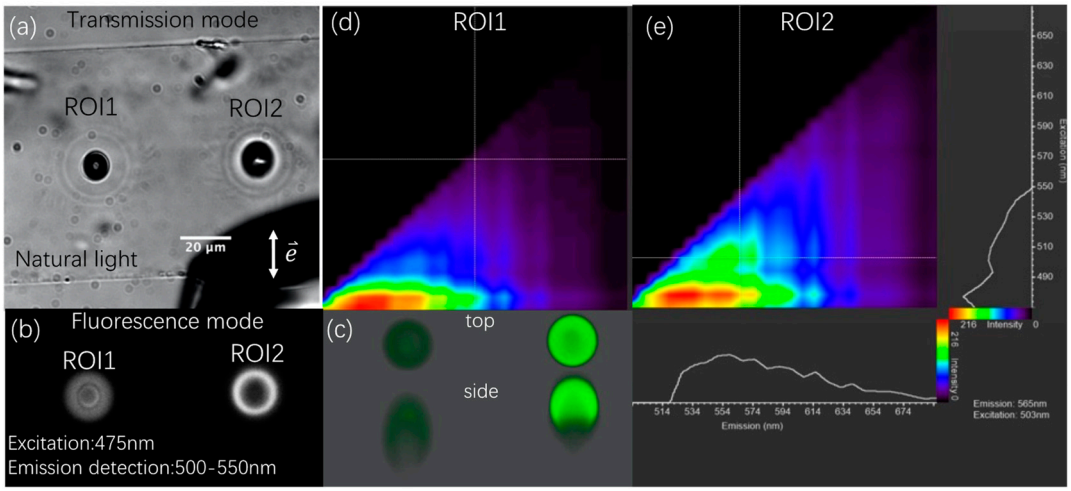

Figure 2. (a) Transmission image of two laser irradiated regions. Parameters of ROI1: 1030nm, 165fs, 10MHz, 51.8 mW, polarization as shown in (a), exposure time of 4s; ROI2: same as ROI1 except two times of extra exposure of 100ms under 18.5mW. (b) fluorescence image of ROI1 and 2. (c) screenshots of 3D model of ROIs on top view and side view. (d)-(e) the excitation-emission matrix of ROIs, on 470-670nm range for the excitation and 494-694nm range for the emission. The color stands for the intensity and interpolation processed by the software, raw data can be found in complementary information.

In addition, the two ROIs were spectroscopically studied in visible range, as illustrated by two excitation emission matrix (EEM) graphs in Figure 2(d) and (e). These graphs reveal the presence of a primary species excited in the range of 470-490nm (red center) in both EEMs thus giving rise to broadband luminescence from green to red. Upon the injection of additional laser energy, ROI2 exhibits a newly generated luminescent center excited at 505nm (see the cross in Figure 2(e)), with emission centered at 560nm. This phenomenon is similar to fs laser-induced PL in Zeonex polymer [36]. Practically, it implies that color alteration can be achieved to a certain extend by modulating the ratio of luminescence excited at 500nm through laser parameters.

Luminescent species excited in UV range. To provide more comprehensive spectral information and to explore potential applications of the luminescent material across different light range, we have characterized its performance in the UV region. Results are shown in Figure 3 and reveal one species excited at 400nm and emits light peak at 474nm.

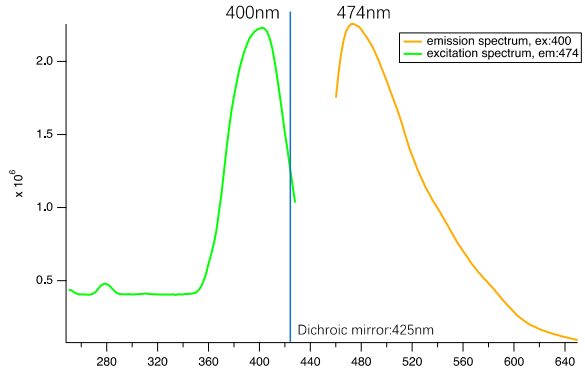

Figure 3. Excitation spectrum in UV range when detection at 474nm (green) and emission spectrum when excited by 400nm continuum laser.

Spatially resolved lifetime of irradiated Type 2. Lifetime measurements serve as a tool to assess variation in the fluorescence yield of the same sample under different conditions of preparation and environment. We have noticed a reproducible and stable fluorescence decay across all samples, with the decays exhibiting multiexponential characteristics as demonstrated in Figure 4c. This behavior

 doi:10.20944/preprints202403.1320.v1

can be attributed to two main factors. Firstly, the fluorescence may originate from a mixture of different species, as in the case of fs laser excitation of electrons, which subsequently recombine to produce carbon dots, which may be of multiple size over a range, their lifetimes span from 6ns down to 2ns. Secondly, the fluorescent molecules are surrounded by non-fluorescent polyaromatic molecules located at fixed random distances from them. In Figure 4(a), the spatial distribution of the fluorescence lifetime (FLIM) highlights a distinct contrast between the center and the edge of a Type 2 fluorescent spots (ROI2 in Figure 2). Specifically, the center displays an average lifetime of 2.5ns, which increases to 3.5ns towards the edge, as depicted in Figure 4(b). This variation could be due to the different nature of the fluorophores formed at different locations in the spot, or to the difference in the concentration of quencher in the center and the edge.

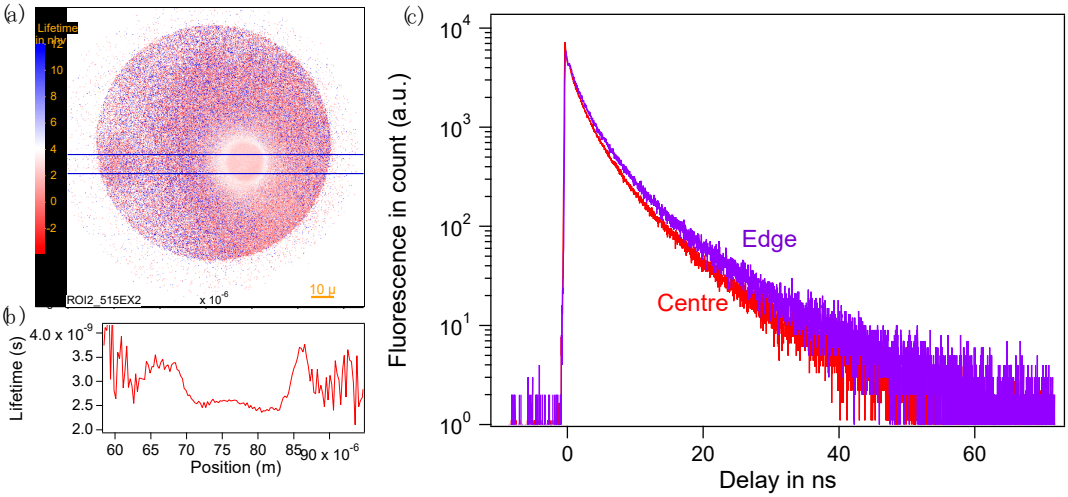

Figure 4. (a) Lifetime distribution of ROI2 (b) Lifetime distribution of ROI2 along the blue horizontal line marked in (a). (c) The fluorescent decay of the center (red) and edge (purple) of ROI2. (d) Lifetime distribution during fs laser irradiation. The laser beam focus located at right side (shorter lifetime with red color).

Spatially resolved lifetime during irradiation by fs laser in scanning mode. To acquire additional insights into the process of luminophore generation, we recorded the lifetime distribution during the fs laser irradiation process. Differ from an irradiation with static mode, the sample was moved from right to left at a speed of 0.1mm/s (refer to Figure 5), while simultaneously being probed by 515nm pulsed light, covering the entire sample. The lifetime image, shown in Figure 5(a), displays a trace with a 'hot spot', corresponding to the laser focal volume. The entire image was collected over 12s, as we can see a trace of 1.2mm in length. PCA analysis reveals that three decays could describe 95% of the luminescence, as depicted in Figure 5(b). With the spatial distribution of these 3 components illustrated in Figure 5 (c), we deduce that (1) The red profile corresponds to luminescence induced by the IR fs laser through a multiphoton excitation process, starting 1.08ns before the other 2 contributions., with an average lifetime of 7.8ns. (2) The green curve represents the luminescence of the trace excited by 515nm laser light, modified by fs laser shortly before, with an average lifetime of 21ns. (3) The blue curve indicates a contribution constantly located around IR focal point over 10µm, excited by 515nm laser light, with an average lifetime of 4.8ns. It is labeled as 'Hot' because it appears only around the focus of the laser beam. Figure 5(d) shows the intensity of these 3 components during irradiation process, measured in photon/s (shown as kHz). The IR fs laser was activated at 1s, presented by a sudden increase in IR induced luminescence (red curve) and the blue curve. Note that in Figure 5(d), the blue curve experienced a sudden increase around 7-8s, lasting around 1s, possibly due to a temporary accumulation triggered by defects.

 doi:10.20944/preprints202403.1320.v1

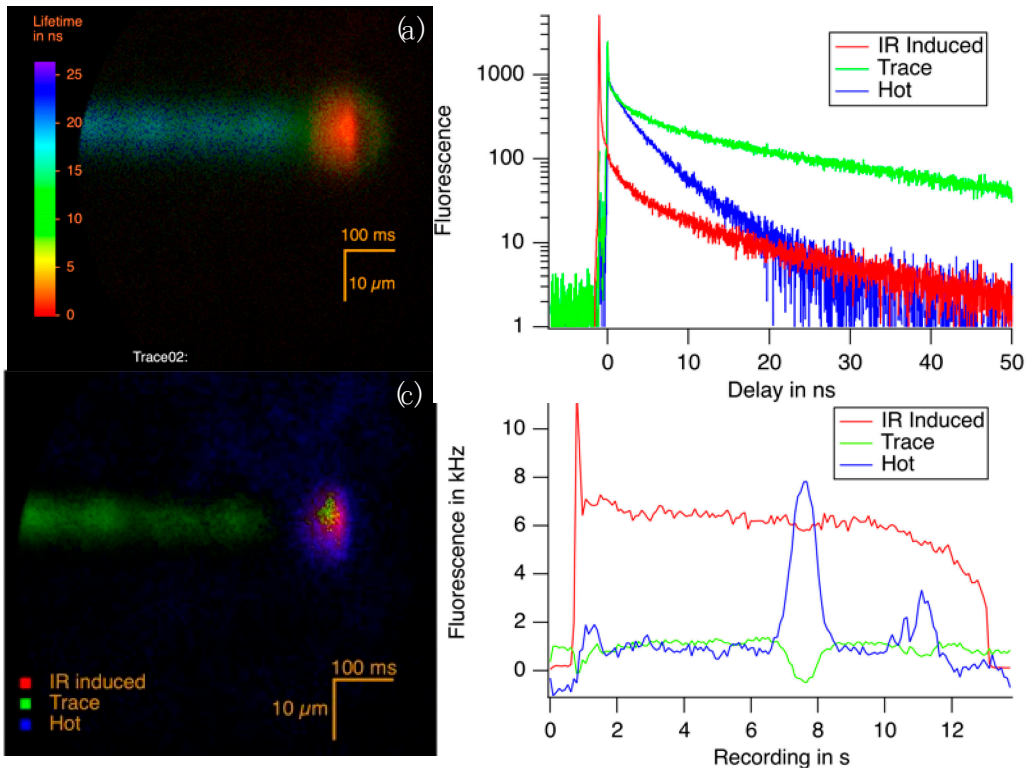

Figure 5. FLIM at the place of irradiation (a) Lifetime distribution during fs laser irradiation. Laser parameters: 5MHz, 40.7mW, scanning speed 100µm/s. The laser beam focus located at right side (shorter lifetime with red color), (b) the three first components of (a), (c) spatial distribution of these 3 components, (d) intensity of these 3 components during irradiation process.

Stabilities in O_2 environment. Type 2 modifications are embedded within the fiber, isolated from the environment, rendering them unsensitive to environmental influences such as pH and oxygen, while Type 3 modifications have an exit connecting to the exterior. It is widely acknowledged that exposure to an oxygen atmosphere can often quenches luminescence, which is a critical consideration in practical application like OLEDs, where creating an oxygen-depleted environment might be necessary. We thus investigated the sensitivity of this luminescence to O_2. For this purpose, we measured the lifetimes of a Type 3 modification, which is exposed to the environment, in both O_2 and Ar atmosphere. The decay profiles are displayed in Figure A1. The result reveals a negligible difference under air, Ar and O_2 environments, suggesting that the observed luminescence is not significantly quenched by oxygen. This inference is drawn from the decay profiles of air does not position itself between the decay curve under Ar and O_2 environment. These laser-induced fluorescent carbon dots are insensitive to the presence of O_2, indicating their potential utility in applications where exposure to oxygen is unavoidable.

3.3. The Identification of Luminescent Region Containing Carbon Dots

The utilization of femtosecond (fs) laser irradiation in the transformation of molecules within a polymer composed solely of carbon and fluorine, resulting in luminescent properties, strongly suggests the formation of carbon-fluorine compounds with aromatic structures. This aligns with numerous studies that have explored the effects of fs laser irradiation on other organic polymers [38,47]. To corroborate our position and further understand the molecule nature of the products formed by laser treatment, we conducted Raman spectroscopy and Transmission Electron Microscopy (TEM) analyses.

Raman spectroscopy. Figure 6 displays the Raman spectra of CYTOP fiber core and the irradiated region corresponding to Type 2 modification, with an insert image showing the measured positions. In the low-wavenumber region of the CYTOP core spectrum (70-800cm^{-1}, orange profile),

 doi:10.20944/preprints202403.1320.v1

the strongest peak at 690cm^{-1} is attributed to aliphatic F-C-F vibrations [48], accompanied by two peaks within 250-350 cm^{-1}. Other peaks in the low-wavenumber region, plus two peaks at 1450 and 1675cm^{-1}, are ascribed to dopants that contribute to the index gradient, details is described in Appendix 1a. The Raman spectrum of Type 2 modified region (blue profile) is characterized by a significant presence with two maxima at 1315cm^{-1} and 1600cm^{-1}, corresponding to G-peak and D-peak of a graphene/graphite carbon-based structure [49,50]. The G peak, typically observed at 1580 cm^{-1}, is associated with the stretching of sp2-hybridized carbon bonds in plane within graphitic structures. D peak, occurring at 1350 cm^{-1}, arises from the breathing mode of sp3-hybridized carbon atoms in disordered or amorphous carbon structures. However, slight shift and broadening of these 2 peaks were noted in our samples, which we hypothesize maybe due to chemical environment such as the presence of fluorine atoms. Similar spectral characteristics, including a more strong D peak relative to G peak, vanishing of the 2D peak, and broadening of both the D peak and G peak, have been reported in oxidized [49,51], fluorinated graphene during the fluorination process [52] and slower scanning speed by fs-induced GQDs.

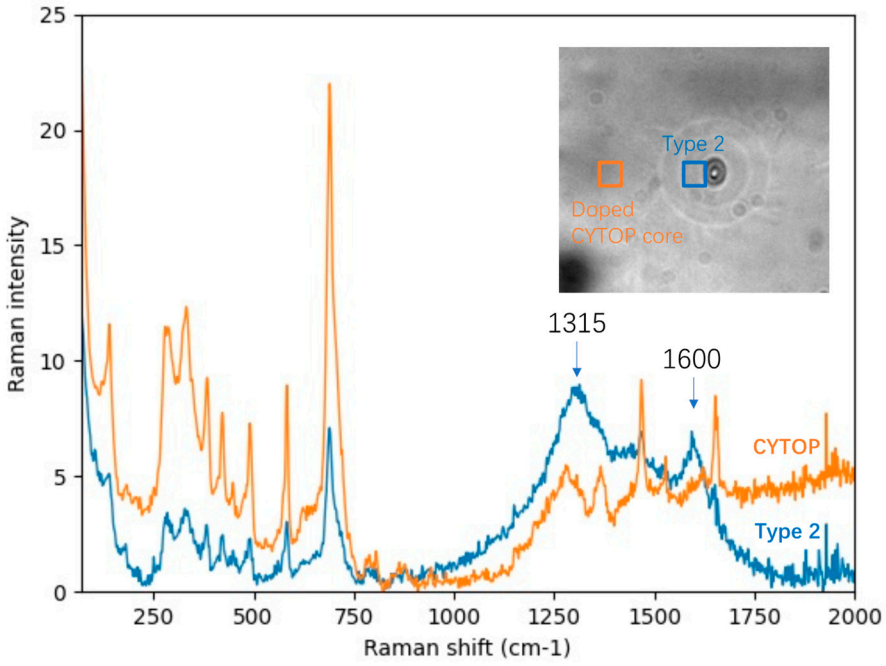

Figure 6. Raman spectra of pristine CYTOP fiber core (orange) and the irradiated region of Type 2 modification (blue). Insert: the measured areas. Laser power for Raman spectroscopy was set to be 10mW, with 20s exposure time and 16-25 times of acquisition, using objective 50x with NA=0.5.

Transmission Electron Microscopy. To elucidate the structural changes induced by femtosecond laser irradiation and understand the formation of luminescent properties within the CYTOP polymer, Transmission Electron Microscopy (TEM) analysis was performed. This method is critical for providing direct visual evidence of the microscopic changes and for validating the nature of modifications at the nanoscale. CYTOP samples were prepared by cutting into thin slices of approximately 70nm. The images shown in Figure 7 offer detailed insights into the modifications. Figure 7(a) displays an overview of a Type 2 modified region, where brighter ellipsoids appear indicating clearly the formation of voids. Figure 7(b)-(d) provide zoomed-in views of different regions marked in Figure 7(a), while Figure 7(e) is a zoom of a region indicated in Figure 7(d). These observations reveal the presence of black dots and voids surrounding the laser-induced void in the Type 2 modification. Those small voids around the central void are indicative of gas production during the irradiation. Notably, the black dots appear smaller, fewer, and shallower the further they

 doi:10.20944/preprints202403.1320.v1

are from the center until about 1-2μm in the periphery. This observation suggests that the luminescence is not a deposition on the inner surface of the void but rather extends around the periphery, within a layer approximately 1-2μm thick. Figure 7(e) displays the details of some black dots, with the size ranging from a few nanometers to tens of nanometers.

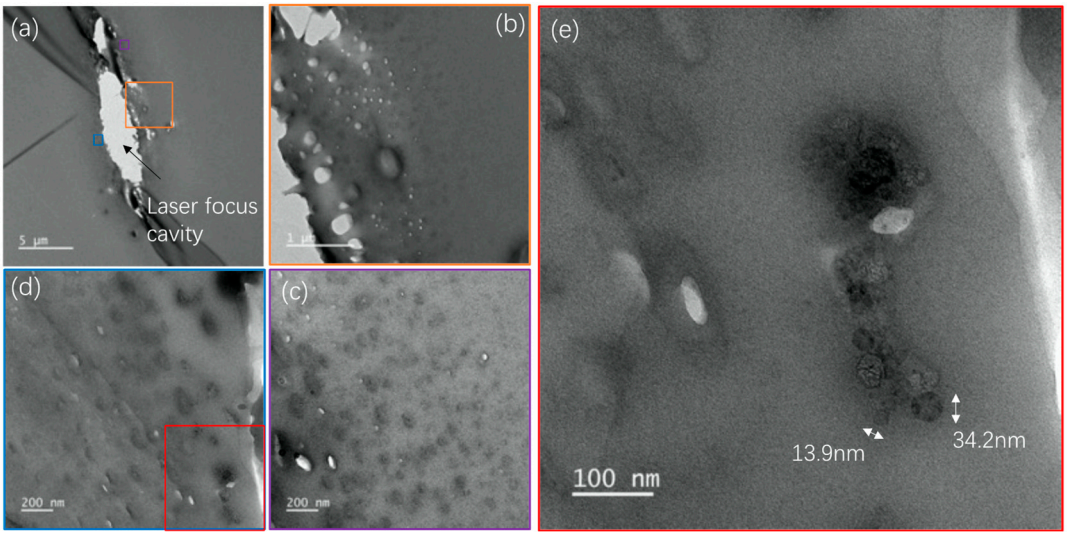

Figure 7. TEM images of Type 2 area irradiated by fs laser of 74mW, 10MHz. the fiber axis is perpendicular to the plan of the photo, (a) A typical cavity in Type 2 modification region. (b) Enlarged image of the area indicated by the orange square in (a). (c) Enlarged image of the area indicated by the purple square in (a). (d) Enlarged image of the area indicated by the blue square in (a). (e) Enlarged image of the area indicated by the red square in (d).

4. Discussion

Kinetic processes of laser-material interaction and carbon dots generation processes. In the discussion, we delve into the kinetic processes involved in the interaction between the laser and material, focusing on the generation of carbon dots within CYTOP, a material with low absorption at 1030nm. Our observations lead us to propose a scenario: when laser irradiates the sample, at the focal point, there is extremely high intensity, the material absorbs partially the pulsed laser energy through multi-photon ionization [53], subsequently leading to the ionization of CYTOP [53]. After about hundreds of milliseconds, a black dot appears at the focal point through natural light transmission observation. This modification that we have quoted Type 1, is likely resulting from transformation of the solid state to a more plastic phase, as we observed a movement of the black dot. With further energy injection, gas generation occurs within milliseconds, transforming the black dot into a void. This void finally increases in volume over irradiation time, and the appearance of rings attributed to sudden volume increase is noted (likely a shock wave) generating a Type 2 modification. Concurrently, carbon dots are formed and distributed, maybe diffused outward around the periphery of the void. Over an extended period, more gas is produced, and its expansion exerts high pressure, enlarging the voids and affecting the surrounding density and may lead to material fracturing. Occasionally, a multifold spiral “galaxy” structure is observed through natural light transmission revealing some twisting of the matter. The origin remains under investigation. It appears also some crystals on the internal surface of the cavity indicating the occurrence of a low viscous phase in the void. Ultimately, this process culminates in a breakthrough to the fiber surface, forming Type 3 modification, with the emergence of a bubble from the newly created tunnel. A comprehensive video detailing this process is available in the supplementary information.

Specifically, in Type 2 modification, the void size increases over exposure time before the transition to type 3. The increase is almost linear, shown in Figure 1(c). The formation of a void in transparent materials at femtosecond laser irradiation is a complex multi-physical phenomenon caused by generation of locally dense plasmas whose recombination brings matter into a highly

 doi:10.20944/preprints202403.1320.v1

stressed state. The geometry of the heat affected zone and the state of the matter in this region (softening, melting, or vaporing) depend on the irradiation parameters where the focusing geometry plays an important role. The most intuitive image of a void formation as Type 2 modification (shown in Figure 1(b)) could be the laser-induced excited electron plasma production that triggers the vaporization of the material in the center, as we have seen the escape of the gas in the latter stages of the process, and melting or softening around, and waveform-like refractive index change. The process is also described in this way under the interaction of a femtosecond laser with polyimide [46]. In addition, some other void formation dynamic has been studied in inorganic materials, silica glass materials e.g., [54–56]. Depending on the materials and irradiation conditions, the formation of cavities is attributed to different scenarios such as spontaneous bubble nucleation in the molten phase [57], high pressures induced by focused laser beams [58], presence of interstitial oxygen, tensile stresses in liquid melt, rapid quenching and so on [55]. In these processes, the temperature distribution appears determining. We thus examine this point below.

Thermal model of laser-matter interaction. After the laser energy deposition at the focus, a heat flow to the surroundings occurs in a few μs. This thermal process can help for understanding the modification induced by fs laser pulses. Here, we computed the temperature fluctuation and evolution over time (until 10μs) at the center and periphery of the beam focus in CYTOP material caused by multi-pulse energy absorption, as shown in Figure 8 (a) and (b). Significant heat accumulation in CYTOP compared to silica glass is expected due to its relatively smaller thermal conductivity. The energy deposition process is considered to be instantaneous. Since the difference between maximum temperature (caused by a pulse deposition) and the minimum temperature (after thermal diffusion within the pulse period) is very small for this RR, we can thus consider a time average temperature everywhere as a reasonable approximation. Figure 8(c) gives the average temperature distribution for different laser power when the thermal system gets to the steady state.

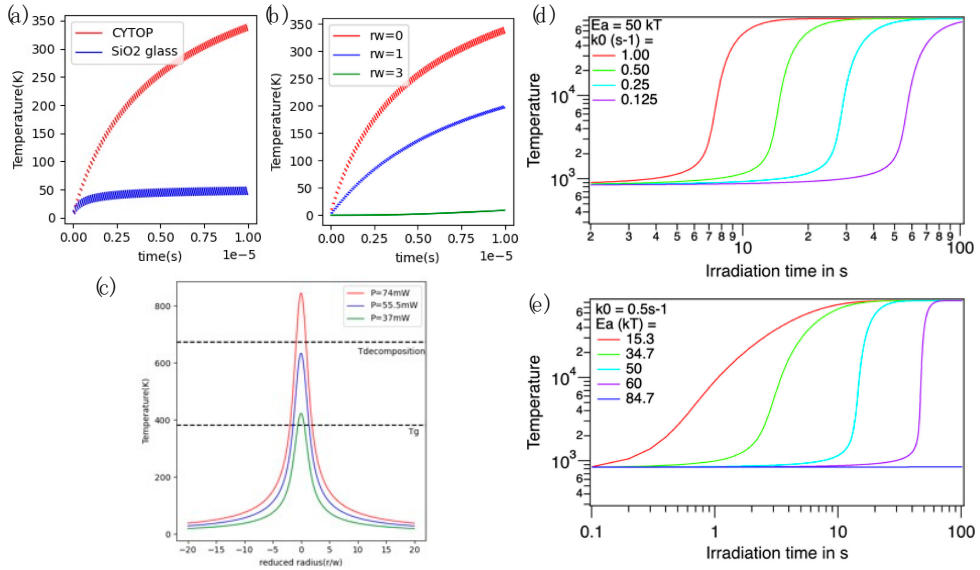

Figure 8. (a) Temperature evolution over time (the origin is room temperature) by 100 laser pulses in a frequency of 10MHz in CYTOP and SiO_2 glass. The parameters of materials are: CYTOP: $\kappa = 0.12\ kg/m^3, \rho = 2030\ J/(kg \cdot K), C_p = 861\ W/(m \cdot K)$ [42]. SiO_2 glass: $\kappa = 1.38\ kg/m^3, \rho = 2203\ J/(kg \cdot K), C_p = 703\ W/(m \cdot K)$ [59], other parameters for both materials: absorption rate A=0.005, laser power 55.5mW, beam radius=0.5μm. (c) Temperature evolution over time at the beam center (reduced radius r_w= r/w =0) and around the center, at r_w=1 and 3. (c) Temperature distribution at steady state with laser power of 37mW, 55mW and 74mW. (d)-(e). Temperature evolution after steady state due to absorption by new species produced lately (second is the time scale) after the initial thermal steady state reaching (the scale is the ms) with (d)same activation energy E_{ai} and different reaction efficiency k_{0i} and (e) different activation energy and same reaction efficiency.

 doi:10.20944/preprints202403.1320.v1

During Type 1 and Type 2 modifications, we observed the material exhibits viscoelastic and plastic behaviors during irradiation, evidenced by the enlargement of cavity and displacement of Type 1 dot. The temperature distribution curves at steady state induced by varying powers were plotted in Figure 8(c). The amplitude of these distributions were based on an absorption rate at A=0.005, chosen for its alignment with the experimental power threshold and the material's key thermal properties, such as glass transition temperature (T_g=381.15K) and decomposition temperature ($T_{decomposition}$=673.15K [42]), shown in black dash lines. With power of 37mW, 55.5mW and 74mW, the temperatures induced by laser pulses result in material no modifications, melting and chemical reaction, respectively. However, this temperature induced by laser pulses can explain the modification threshold but not the reasons behind the cavity size change over exposure time. In Type 2 modification, the void size and its exposure time dependence are not directly related to the temperature affected zone, because firstly, a steady state is reached in less than 3ms (calculation details are in Appendix 3 and [60]), the exposure time arising from 500ms to 1s should not change the laser-induced temperature. Secondly, the void size is larger than the heat affected width shown in Figure 8(c). Therefore, this may indicate that new molecules induced by the laser can continuously absorb the laser energy to produce a new round of temperature rising, and if it contains gas, the volume is enlarged. Figure 8 (d) and (e) shows at larger time scale a temperature evolution until 100s based on this process, Figure 8(a) is involved in this profile as an invisible step from 0 to the lowest value at the beginning (0-10μs). Then, we have assumed a simple laser induced chemical reaction from A to B_i with a constant rate k_{0i} and activation energy Ea_i that allows placing the half time of the reaction (advancement degree=1/2) in the second time scale, as shown in Figure 8 (d) and (e). Figure 8 (d) and (e) display the temperature evolution induced by these chemical reactions according to reaction rate k_{0i} and activation energy Ea_i. Results demonstrate that both Ea and k_0 influence the incubation time, while the temperature slope is influenced by Ea.

Commonality on spectral properties. We found a specific distribution of luminescent species across several laser-modified organic materials, including glycine singe crystal [37], Zeonex [36], and even caramelized sucrose. This finding suggests a commonality in chemical structures of the luminescent species generated by femtosecond laser in these organic materials, possibly related to a similar size of carbon dots. The presence of fluorescent species at 475nm excitation indicates that the size of the carbon dots produced falls within a favorable range. This is supported by reports showing that the HOMO-LUMO gap is strongly affected by the size of GQDs [61–63]. TD-DFT calculation revealed that the absorption wavelengths of the pristine GQDs vary with size, ranging from 168.06nm to 507.86nm, correlating with sizes from 0.27nm to 1.43nm, or from C6 to C76 [62], consistent with experimental observation [64,65]. Based on that, the carbon dots with absorption at 400nm, 475nm and 520nm produced with higher energy deposition, are estimated to have sizes around 1.1nm, 1.4nm and 1.5nm with approximately 5 phenyl rings. In addition, Ma et al. [66] separated caramel into low and high molecular weight portions by dialysis, discovering blue fluorescence under UV light in former, which indicates that the fluorescent species are small molecules. However, further investigation is needed to understand why laser-induced species in organic materials tend to be of this specific size range.

5. Conclusions

CYTOP fiber, composed only carbon, fluorine, and oxygen atomes, exhibits low attenuation in visible-IR range compared to other polymers. We have successfully synthesized luminescent perfluorinated CDs within the core of this optical fiber for the first time, through a simple, efficient light-based method, known as FLDW. We have identified an optimal set of laser parameters and developed a 'combo irradiation' that enable to produce luminescent species with a good efficiency. These laser-induced CDs has at least 3 excitation centers from UV to visible range, exhibiting efficient emission from the green to the red spectral range. Additionally, the light dose influences not only the PL intensity, but also the cavity size, which can be utilized to control optical polarization. Our thermal and chemical modelling indicates that the cavity size, itself, is influenced not only by laser energy deposition but also by the induced species absorbing the laser light more efficiently through

 doi:10.20944/preprints202403.1320.v1

subsequent chemical reaction, thereby increasing the temperature over a larger radius around the initial voids. Moreover, functionalization of CYTOP optical fibers with CDs holds promise for application such as luminescence-based fiber sensing, stimulator, and UV down converters. Its insensitivity to oxygen may contribute to achieve durable devices. Furthermore, our study highlights the potential of FLDW as an eco-friendly and efficient processing technique for selectively synthesizing CDs with novel properties and applications.

Supplementary Materials: The following supporting information can be downloaded at the website of this paper posted on Preprints.org.

Author Contributions: R.Q, B.P, M.L. and R.B.P conceived the project. Experimental acquisitions were performed by R.Q with great support of J-F.A, E.G-C, and O.P. R.Q, B.P and R.B.P contributed to the manuscript writing, thermal simulation, data analysis and treatment. M.L and K.K provided fiber materials and information.

Acknowledgments: This work was supported by CHARMMMAT ANR-11-IDEX-0003-02. We are grateful to Christophe Sandt and Ferenc Borondics of SMIS group of Soleil synchrotron for providing Raman spectroscopy system and information. The EEM and TEM experiments benefited from Imagerie-Gif core facility supported by l'Agence Nationale de la Recherche (ANR-11-EQPX-0029/Morphoscope, ANR-10-INBS-04/FranceBioImaging; ANR-11-IDEX-0003-02/ Saclay Plant Sciences).

Appendix 1

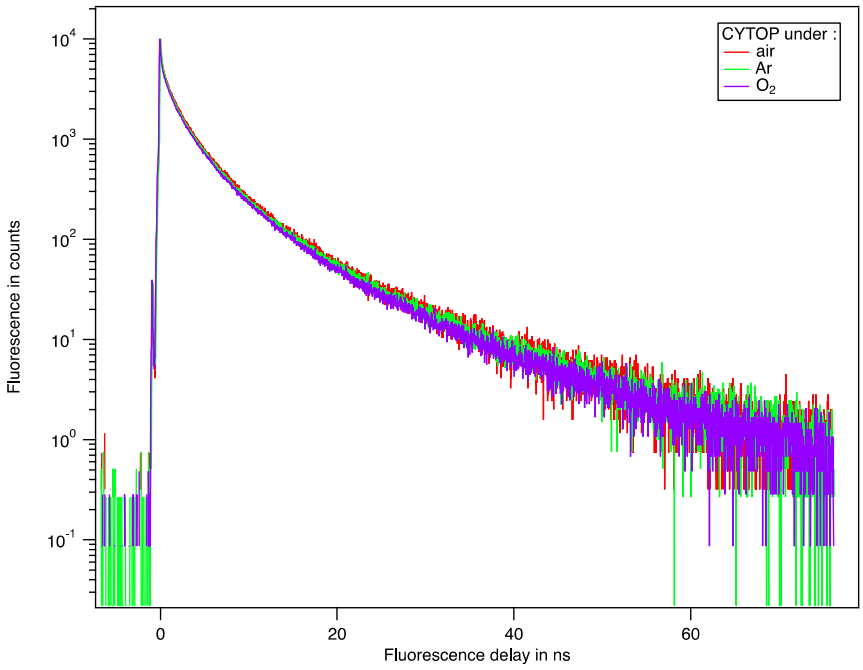

Figure A1. Fluorescence decay in air, O_2 and Ar environment.

Appendix 2

Composition Analysis of the CYTOP Fiber and Carbon Dots from the Raman Spectra

Two families of spectra were collected and analyzed using Principal Component Analysis (PCA), a technique aiming at identifying and constructing a minimal set of spectra that properly represent the data. One family was collected at different positions within the pristine fibers (fiber core and cladding). The cladding is expected to be composed solely by CYTOP material, while the core should contain both CYTOP material (pure and doped), for providing refractive index gradient. The acquired spectra have stable and consistent structures, with two exemplary spectra displayed in Figure A2(a). Figure A2(b) shows the 3 principal components CP0, CP1 and CP2, describing 98% of the spectra of the pristine fiber. As indicated by the red profile (CP0), peaks at 290cm^{-1}, 335cm-1 cm^{-1}, 690cm-1 cm^{-1} originate from the pure CYTOP polymer, with the most pronounced peak at 690cm^{-1}

Preprints.org (www.preprints.org) | NOT PEER-REVIEWED | Posted: 22 March 2024 doi:10.20944/preprints202403.1320.v1

being attributed to the aliphatic F-C-F vibration [1]. The spectrum CP1 is identified as belonging to an aromatic perfluorinated compound, with the peak at 584cm^{-1} corresponding to the Φ-F bound [2], associated with peaks at 1450 and 1675cm^{-1} peaks are attributed to the dopants.

The second family with 36 spectra of different modifications and regions (5 pristine, 2 type 1, 17 type 2, 12 Type 3) was collected, with 4 spectra examples displayed in Figure A2(c). Spectra of Type 1 modification exhibit the same feature as the unirradiated CYTOP fiber material. Type 2 spectra show a decrease in the CYTOP structure signal, but an emergence of graphene features, including identical D-peak and G-peak. In Type 3 spectra, the CYTOP signal almost disappears, with the two graphene peaks overall elevated and exhibit a flatten profile. The spectra CP0, CP1 and CP2 from PCA analysis, as shown in Figure A2(d), describe 75% of the data. The spectrum CP0, CP1 and CP2 are interpreted to originate from CYTOP+dopants, graphene structure and fluorescence of the CDs excited at 780nm, respectively.

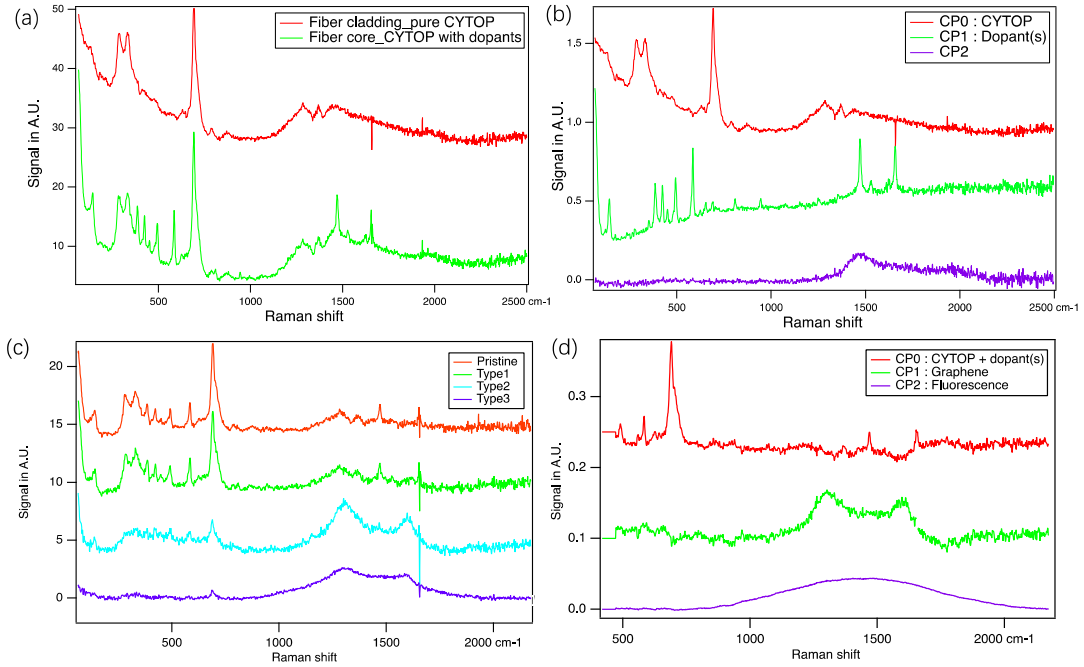

Figure A2. (a) Raman spectra of CYTOP fiber cladding (red) and core (green). (b) The first 3 major components by PCA, representing pure CYTOP (red), doped (green), and unknow fluorescent molecule(s) in the fiber (c) Raman spectra of pristine CYTOP (red), Type 1 modification (green), Type 2 modifications (blue) and Type 3 modifications (purple). (d) type 2 PCA first 3 major components.

Appendix 3 (Information Extracted from [3])

N is the pulse number, pulse period $\tau_p = 0.1\mu s$, beam radius w=0.5μm at 1/e, thermal diffusion time $\tau_D = 2.78\mu s$, $R_\tau = 0.036$, due to this low value, the T oscillations are very small and the heat accumulation very large, spherical focus voxel, reduced radius r_w=r/w. The use of temperature averaging is thus justified and simpler.

We define a time averaging of the temperature by $\bar{T}(r_w, N) = \frac{1}{\tau_p}\int_{\substack{pulse\ period \\ at\ N}} T(r_w, t)\, dt$, where

$$T(r_w,t) = T_{00} \sum_{n=0}^{N-1=\text{integer part}\left(\frac{t}{\tau_p}\right)} \frac{1}{\left[1+\left(\frac{t}{\tau_{RR}}-n\right).R_\tau\right]^{\frac{3}{2}}}.\exp\left[-\frac{(r_w)^2}{1+\left(\frac{t}{\tau_{RR}}-n\right).R_\tau}\right], with\ T_{00} = \frac{A\cdot E_p}{\pi^{\frac{3}{2}}\cdot\rho\cdot C_p(w)^3}, R_\tau = \frac{\tau_{RR}}{\tau_d}$$

The integral yields the final temperature limit in steady state when $N \to \infty$:

$$\bar{T}(r_w) = \frac{\sqrt{\pi}}{R_\tau.\ r_w} erf(r_w)\, T_{00}$$

$erf(r_w)$ is the error function. When $r_w = 0, \bar{T}(0) = \frac{2}{R_\tau.} T_{00}, r_w > 2, \bar{T}(r_w) = \frac{\sqrt{\pi}}{R_\tau.\ r_w}$.

 doi:10.20944/preprints202403.1320.v1

For the time we consider (larger than 0.1s at 10MHz), steady state is reached largely, i.e. the residual temperature increase is negligible, (amounting a few % e.g. 6%, this is ε in the next formula). As a matter of fact, the needed pulse number is calculated to be:

$N_{ss}^{\mathrm{r}} > \frac{1}{R_\tau}\left[\left(\frac{2.r_w}{\varepsilon\sqrt{\pi}.erf(r_w)}\right)^2 - 1\right]$, and $N_{ss}^{0} > \frac{1}{R_\tau}\left[\left(\frac{1}{\varepsilon}\right)^2 - 1\right]$ e.g., when $r_w = 0$, $N_{ss}^{\mathrm{r}} = 7689$

This value is much smaller than the minimum number of pulses deposited (>10^6).

And, the time to reach the steady state is estimated to be $N_{ss}^{\mathrm{r}} \cdot \tau_{RR}$:

$t_{ss}^{\mathrm{r}} > \tau_d\left[\left(\frac{2.r_w}{\varepsilon\sqrt{\pi}.erf(r_w)}\right)^2 - 1\right]$, and $t_{ss}^{0} > \tau_d\left[\left(\frac{1}{\varepsilon}\right)^2 - 1\right]$ e.g., when $r_w = 0$, $t_{ss}^{\mathrm{r}} = 769\mu s$

i.e. less than 1ms.

References

1. S. Zhu, Y. Song, X. Zhao, J. Shao, J. Zhang, and B. Yang, "The photoluminescence mechanism in carbon dots (graphene quantum dots, carbon nanodots, and polymer dots): current state and future perspective," Nano Research **8**, 355-381 (2015).
2. X. Xu, R. Ray, Y. Gu, H. J. Ploehn, L. Gearheart, K. Raker, and W. A. Scrivens, "Electrophoretic analysis and purification of fluorescent single-walled carbon nanotube fragments," Journal of the American Chemical Society **126**, 12736-12737 (2004).
3. J. E. Riggs, Z. Guo, D. L. Carroll, and Y.-P. Sun, "Strong luminescence of solubilized carbon nanotubes," Journal of the American Chemical Society **122**, 5879-5880 (2000).
4. S. Kargozar, S. J. Hoseini, P. B. Milan, S. Hooshmand, H. W. Kim, and M. Mozafari, "Quantum dots: a review from concept to clinic," Biotechnology Journal **15**, 2000117 (2020).
5. G. Vargas-Nadal, M. Kober, A. Nsamela, F. Terenziani, C. Sissa, S. Pescina, F. Sonvico, A. M. Gazzali, H. A. Wahab, L. Grisanti, M. E. Olivera, M. C. Palena, M. L. Guzman, L. C. Luciani-Giacobbe, A. Jimenez-Kairuz, N. Ventosa, I. Ratera, K. D. Belfield, and B. M. Maoz, "Fluorescent Multifunctional Organic Nanoparticles for Drug Delivery and Bioimaging: A Tutorial Review," Pharmaceutics **14**(2022).
6. J. Geys, A. Nemmar, E. Verbeken, E. Smolders, M. Ratoi, M. F. Hoylaerts, B. Nemery, and P. H. Hoet, "Acute toxicity and prothrombotic effects of quantum dots: impact of surface charge," Environ Health Perspect **116**, 1607-1613 (2008).
7. M. Li, T. Chen, J. J. Gooding, and J. Liu, "Review of Carbon and Graphene Quantum Dots for Sensing," ACS Sensors **4**, 1732-1748 (2019).
8. B. Wang, H. Cai, G. I. N. Waterhouse, X. Qu, B. Yang, and S. Lu, "Carbon Dots in Bioimaging, Biosensing and Therapeutics: A Comprehensive Review," Small Science **2**(2022).
9. S. Bayda, E. Amadio, S. Cailotto, Y. Frion-Herrera, A. Perosa, and F. Rizzolio, "Carbon dots for cancer nanomedicine: a bright future," Nanoscale Adv **3**, 5183-5221 (2021).
10. M. Han, S. Zhu, S. Lu, Y. Song, T. Feng, S. Tao, J. Liu, and B. Yang, "Recent progress on the photocatalysis of carbon dots: Classification, mechanism and applications," Nano Today **19**, 201-218 (2018).
11. Q. Zeng, D. Shao, X. He, Z. Ren, W. Ji, C. Shan, S. Qu, J. Li, L. Chen, and Q. Li, "Carbon dots as a trackable drug delivery carrier for localized cancer therapy in vivo," J Mater Chem B **4**, 5119-5126 (2016).
12. H. Ding, S. B. Yu, J. S. Wei, and H. M. Xiong, "Full-Color Light-Emitting Carbon Dots with a Surface-State-Controlled Luminescence Mechanism," ACS Nano **10**, 484-491 (2016).
13. T. Feng, S. Tao, D. Yue, Q. Zeng, W. Chen, and B. Yang, "Recent Advances in Energy Conversion Applications of Carbon Dots: From Optoelectronic Devices to Electrocatalysis," Small **16**, e2001295 (2020).
14. W. Shang, T. Cai, Y. Zhang, D. Liu, and S. Liu, "Facile one pot pyrolysis synthesis of carbon quantum dots and graphene oxide nanomaterials: All carbon hybrids as eco-environmental lubricants for low friction and remarkable wear-resistance," Tribology International **118**, 373-380 (2018).
15. F. J. Chao-Mujica, L. Garcia-Hernández, S. Camacho-López, M. Camacho-López, M. A. Camacho-López, D. Reyes Contreras, A. Pérez-Rodríguez, J. P. Peña-Caravaca, A. Páez-Rodríguez, J. G. Darias-Gonzalez, L. Hernandez-Tabares, O. Arias de Fuentes, E. Prokhorov, N. Torres-Figueredo, E. Reguera, and L. F. Desdin-García, "Carbon quantum dots by submerged arc discharge in water: Synthesis, characterization, and mechanism of formation," Journal of Applied Physics **129**(2021).
16. X. Liu, J. Pang, F. Xu, and X. Zhang, "Simple Approach to Synthesize Amino-Functionalized Carbon Dots by Carbonization of Chitosan," Sci Rep **6**, 31100 (2016).
17. D. Zhang, D. Chao, C. Yu, Q. Zhu, S. Zhou, L. Tian, and L. Zhou, "One-Step Green Solvothermal Synthesis of Full-Color Carbon Quantum Dots Based on a Doping Strategy," The Journal of Physical Chemistry Letters **12**, 8939-8946 (2021).
18. M. R. Hasan, N. Saha, T. Quaid, and M. T. Reza, "Formation of Carbon Quantum Dots via Hydrothermal Carbonization: Investigate the Effect of Precursors," Energies **14**(2021).

19. Y. Guo and W. Zhao, "Hydrothermal synthesis of highly fluorescent nitrogen-doped carbon quantum dots with good biocompatibility and the application for sensing ellagic acid," Spectrochimica Acta Part A: Molecular and Biomolecular Spectroscopy **240**, 118580 (2020).
20. Y. Xie, J. Zheng, Y. Wang, J. Wang, Y. Yang, X. Liu, and Y. Chen, "One-step hydrothermal synthesis of fluorescence carbon quantum dots with high product yield and quantum yield," Nanotechnology **30**, 085406 (2019).
21. Y. Wang, X. Chang, N. Jing, and Y. Zhang, "Hydrothermal synthesis of carbon quantum dots as fluorescent probes for the sensitive and rapid detection of picric acid," Analytical Methods **10**, 2775-2784 (2018).
22. Y. Liu, W. Li, P. Wu, C. Ma, X. Wu, M. Xu, S. Luo, Z. Xu, and S. Liu, "Hydrothermal synthesis of nitrogen and boron co-doped carbon quantum dots for application in acetone and dopamine sensors and multicolor cellular imaging," Sensors and Actuators B: Chemical **281**, 34-43 (2019).
23. P. A. N. de Yro, G. M. O. Quaichon, R. A. T. Cruz, C. S. Emolaga, M. C. O. Que, E. R. Magdaluyo, Jr, and B. A. Basilia, "Hydrothermal synthesis of carbon quantum dots from biowaste for bio-imaging," AIP Conference Proceedings **2083**(2019).
24. R. Atchudan, T. N. Jebakumar Immanuel Edison, M. Shanmugam, S. Perumal, T. Somanathan, and Y. R. Lee, "Sustainable synthesis of carbon quantum dots from banana peel waste using hydrothermal process for in vivo bioimaging," Physica E: Low-dimensional Systems and Nanostructures **126**, 114417 (2021).
25. A. Kumar, I. Kumar, and A. K. Gathania, "Synthesis, characterization and potential sensing application of carbon dots synthesized via the hydrothermal treatment of cow milk," Scientific Reports **12**, 22495 (2022).
26. P. Yang, Z. Zhu, M. Chen, W. Chen, and X. Zhou, "Microwave-assisted synthesis of xylan-derived carbon quantum dots for tetracycline sensing," Optical Materials **85**, 329-336 (2018).
27. S. K. Das, R. Gawas, S. Chakrabarty, G. Harini, R. Patidar, and K. Jasuja, "An Unexpected Transformation of Organic Solvents into 2D Fluorescent Quantum Dots during Ultrasonication-Assisted Liquid-Phase Exfoliation," The Journal of Physical Chemistry C **123**, 25412-25421 (2019).
28. G. Jiang, T. Jiang, H. Zhou, J. Yao, and X. Kong, "Preparation of N-doped carbon quantum dots for highly sensitive detection of dopamine by an electrochemical method," RSC Advances **5**, 9064-9068 (2015).
29. X. Feng and Y. Zhang, "A simple and green synthesis of carbon quantum dots from coke for white light-emitting devices," RSC Advances **9**, 33789-33793 (2019).
30. Q. Tan, R. Zhang, G. Zhang, X. Liu, F. Qu, and L. Lu, "Embedding carbon dots and gold nanoclusters in metal-organic frameworks for ratiometric fluorescence detection of Cu(2)," Anal Bioanal Chem **412**, 1317-1324 (2020).
31. H. M. Gonçalves, A. J. Duarte, F. Davis, S. P. Higson, and J. C. E. da Silva, "Layer-by-layer immobilization of carbon dots fluorescent nanomaterials on single optical fiber," Analytica chimica acta **735**, 90-95 (2012).
32. Y. Shimotsuma, P. G. Kazansky, J. Qiu, and K. Hirao, "Self-Organized Nanogratings in Glass Irradiated by Ultrashort Light Pulses," Physical Review Letters **91**, 247405 (2003).
33. Q. Xie, M. Cavillon, D. Pugliese, D. Janner, B. Poumellec, and M. Lancry, "On the Formation of Nanogratings in Commercial Oxide Glasses by Femtosecond Laser Direct Writing," Nanomaterials **12**, 2986 (2022).
34. J. Cao, M. Lancry, F. Brisset, L. Mazerolles, R. Saint-Martin, and B. Poumellec, "Femtosecond laser-induced crystallization in glasses: growth dynamics for orientable nanostructure and nanocrystallization," Crystal Growth & Design **19**, 2189-2205 (2019).
35. K. L. N. Deepak, R. Kuladeep, S. Venugopal Rao, and D. Narayana Rao, "Luminescent microstructures in bulk and thin films of PMMA, PDMS, PVA, and PS fabricated using femtosecond direct writing technique," Chemical Physics Letters **503**, 57-60 (2011).
36. R. Que, L. Houel-Renault, M. Temagoult, C. Herrero, M. Lancry, and B. Poumellec, "Space-selective creation of photonics functions in a new organic material: Femtosecond laser direct writing in Zeonex glass of refractive index change and photoluminescence," Optical Materials **133**, 112651 (2022).
37. R. Que, L. Houel-Renault, M. Lancry, M. Fontaine-Aupart, T. Nait, and B. Poumellec, "Space-selective Luminescence Creation in Organic Crystal by Femtosecond Laser Irradiation," in *Integrated Photonics Research, Silicon and Nanophotonics*, (Optica Publishing Group, 2020), ITu4A. 9.
38. A. A. Astafiev, A. M. Shakhov, A. A. Osychenko, M. S. Syrchina, A. V. Karmenyan, U. A. Tochilo, and V. A. Nadtochenko, "Probing intracellular dynamics using fluorescent carbon dots produced by femtosecond laser in situ," ACS omega **5**, 12527-12538 (2020).
39. S. Kim, K. Suzuki, A. Sugie, H. Yoshida, M. Yoshida, and Y. Suzuki, "Effect of end group of amorphous perfluoro-polymer electrets on electron trapping," Science and Technology of advanced MaTerialS **19**, 486-494 (2018).
40. A. Yeniay, R. Gao, K. Takayama, R. Gao, and A. F. Garito, "Ultra-low-loss polymer waveguides," Journal of lightwave technology **22**, 154-158 (2004).
41. M. Naritomi, H. Murofushi, and N. Nakashima, "Dopants for a Perfluorinated Graded Index Polymer Optical Fiber," Bulletin of the Chemical Society of Japan **77**, 2121-2127 (2004).

42. https://www.agc-chemicals.com/file.jsp?id=jp/en/fluorine/products/cytop/download/pdf/CYTOP_EN_Brochure.pdf.
43. H. P. A. van den Boom, W. Li, P. K. van Bennekom, I. T. Monroy, and K. Giok-Djan, "High-capacity transmission over polymer optical fiber," IEEE Journal of Selected Topics in Quantum Electronics **7**, 461-470 (2001).
44. G. P. Association, *Physical properties of glycerine and its solutions* (Glycerine Producers' Association, 1963).
45. J. A. Spitz, R. Yasukuni, N. Sandeau, M. Takano, J. J. Vachon, R. Méallet-Renault, and R. B. Pansu, "Scanning-less wide-field single-photon counting device for fluorescence intensity, lifetime and time-resolved anisotropy imaging microscopy," Journal of microscopy **229**, 104-114 (2008).
46. D. L. N. Kallepalli, A. T. K. Godfrey, J. Walia, F. Variola, A. Staudte, C. Zhang, Z. J. Jakubek, and P. B. Corkum, "Multiphoton laser-induced confined chemical changes in polymer films," Opt Express **28**, 11267-11279 (2020).
47. S. Hayashi, K. Tsunemitsu, and M. Terakawa, "Laser Direct Writing of Graphene Quantum Dots inside a Transparent Polymer," Nano Lett **22**, 775-782 (2022).
48. F. A. Miller and B. M. Harney, "The infrared and Raman spectra of perfluorocyclohexane," Spectrochimica Acta Part A: Molecular Spectroscopy **28**, 1059-1066 (1972).
49. I. Childres, L. A. Jauregui, W. Park, H. Cao, and Y. P. Chen, "Raman spectroscopy of graphene and related materials," New developments in photon and materials research **1**, 1-20 (2013).
50. D. Sfyris, G. Sfyris, and C. Galiotis, "Stress intrepretation of graphene E-2g and A-1g vibrational modes: theoretical analysis," arXiv preprint arXiv:1706.04465 (2017).
51. I. Childres, L. A. Jauregui, J. Tian, and Y. P. Chen, "Effect of oxygen plasma etching on graphene studied using Raman spectroscopy and electronic transport measurements," New Journal of Physics **13**(2011).
52. R. R. Nair, W. Ren, R. Jalil, I. Riaz, V. G. Kravets, L. Britnell, P. Blake, F. Schedin, A. S. Mayorov, and S. Yuan, "Fluorographene: a two-dimensional counterpart of Teflon," small **6**, 2877-2884 (2010).
53. C. B. Schaffer, A. Brodeur, and E. Mazur, "Laser-induced breakdown and damage in bulk transparent materials induced by tightly focused femtosecond laser pulses," Measurement Science and Technology **12**, 1784 (2001).
54. M. Beresna, M. Gecevičius, N. M. Bulgakova, and P. G. Kazansky, "Twisting light with micro-spheres produced by ultrashort light pulses," Opt. Express **19**, 18989-18996 (2011).
55. K. Cvecek, I. Miyamoto, and M. Schmidt, "Gas bubble formation in fused silica generated by ultra-short laser pulses," Opt. Express **22**, 15877-15893 (2014).
56. E. N. Glezer and E. Mazur, "Ultrafast-laser driven micro-explosions in transparent materials," Applied Physics Letters **71**, 882-884 (1997).
57. Y. Bellouard and M.-O. Hongler, "Femtosecond-laser generation of self-organized bubble patterns in fused silica," Opt. Express **19**, 6807-6821 (2011).
58. S. Juodkazis, K. Nishimura, S. Tanaka, H. Misawa, E. G. Gamaly, B. Luther-Davies, L. Hallo, P. Nicolai, and V. T. Tikhonchuk, "Laser-induced microexplosion confined in the bulk of a sapphire crystal: evidence of multimegabar pressures," Physical review letters **96**, 166101 (2006).
59. https://www.crystran.co.uk/optical-materials/silica-glass-sio2.
60. R. Que, M. Lancry, and B. Poumellec, "Usable Analytical Expressions for Temperature Distribution Induced by Ultrafast Laser Pulses in Dielectric Solids," Micromachines **15**(2024).
61. S. Sarkar, D. Gandla, Y. Venkatesh, P. R. Bangal, S. Ghosh, Y. Yang, and S. Misra, "Graphene quantum dots from graphite by liquid exfoliation showing excitation-independent emission, fluorescence upconversion and delayed fluorescence," Phys Chem Chem Phys **18**, 21278-21287 (2016).
62. M. Yang, Z. Lian, C. Si, and B. Li, "Revealing the role of nitrogen dopants in tuning the electronic and optical properties of graphene quantum dots via a TD-DFT study," Phys Chem Chem Phys **22**, 28230-28237 (2020).
63. K. Müllen, "Evolution of Graphene Molecules: Structural and Functional Complexity as Driving Forces behind Nanoscience," ACS Nano **8**, 6531-6541 (2014).
64. J. W. Patterson, "The ultraviolet absorption spectra of coronene," Journal of the American Chemical Society **64**, 1485-1486 (1942).
65. E. Clar and W. Schmidt, "Correlations between photoelectron and ultraviolet absorption spectra of polycyclic hydrocarbons: the terrylene and peropyrene series," Tetrahedron **34**, 3219-3224 (1978).
66. J. Ma, L. Bian, L. Zhao, X. Feng, L. Zhao, Z. Wang, and Q. Pu, "Dialysed caramel as an effective fluorophore for the simultaneous detection of three nitrophenols," Talanta **197**, 159-167 (2019).
67. F. A. Miller and B. M. Harney, "The infrared and Raman spectra of perfluorocyclohexane," Spectrochimica Acta Part A: Molecular Spectroscopy 28, 1059-1066 (1972).
68. C. M. Sharts, V. S. Gorelik, A. Agoltsov, L. I. Zlobina, and O. N. Sharts, "Detection of carbon-fluorine bonds in organofluorine compounds by Raman spectroscopy using a copper-vapor laser," in *Electro-Optic, Integrated Optic, and Electronic Technologies for Online Chemical Process Monitoring*, (SPIE, 1999), 317-326.

 doi:10.20944/preprints202403.1320.v1

69. R. Saito, M. Hofmann, G. Dresselhaus, A. Jorio, and M. S. Dresselhaus, "Raman spectroscopy of graphene and carbon nanotubes," Advances in Physics **60**, 413-550 (2011).
70. R. Que, M. Lancry, and B. Poumellec, "Usable Analytical Expressions for Temperature Distribution Induced by Ultrafast Laser Pulses in Dielectric Solids," Micromachines **15**(2024).